CrystEngComm

Accepted Manuscript

ROYAL SOCIETY OF CHEMISTRY

www.rsc.org/crystengcomm

Table of Contents

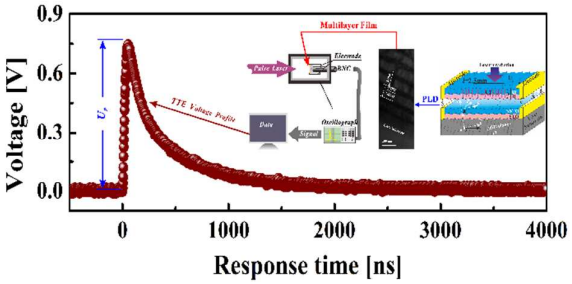

The TTE voltage effect has been greatly improved by constructing the artificial multilayer structure of STO/NSTO with accurate inclined orientation.

Journal Name

RSCPublishing

ARTICLE

Development of transverse thermoelectric voltage effect in artificial $SrTiO_3/SrTi_{1-x}Nb_xO_3$ epitaxial multilayer films with incline-oriented sublayers

Cite this: DOI: 10.1039/x0xx00000x

Received 00th January 2012,
Accepted 00th January 2012

DOI: 10.1039/x0xx00000x

www.rsc.org/

Yi Qin,[a] Ting Zhao,[a] Bo Wang,*[a] Pengxiang Zhang[bc] and Jianfeng Yang*[a]

Artificial $SrTiO_3/SrTi_{1-x}Nb_xO_3$ multilayer films were epitaxially grown on 10° off-cut (001) $LaAlO_3$ single crystal substrates by pulsed laser deposition. The microstructural characterizations by X-ray diffraction and high resolution transmission electron microscopy indicated that the multilayer films were periodic modulation structure with atomically sharp interfaces and inclined *c*-axis oriented. All sublayers with inclined (001) planes were exactly tilted away from the interfaces by the same 10°. The unique transverse thermoelectric voltage signals were achieved up to 0.744 V in the multilayer films, which is hundreds times larger than the bulk Nb-doped $SrTiO_3$ (~ 3 mV) single crystals with the same inclined orientation. The response time of the signals, depending on the thermal relaxation process in this multilayer structure, increased exponentially from 600 ns to 1700 ns with increasing the thickness of $SrTi_{1-x}Nb_xO_3$ sublayer. Furthermore, the peak value of voltage presented a significant linear relationship with the energy absorbed by the film. The results demonstrated that the transverse thermoelectric voltage effect was improved in these films due to their multilayer structure with inclined crystal orientation, which would expand the possibilities of thermoelectric devices for versatile applications.

Introduction

Transverse thermoelectric (TTE) voltage effect was first found and demonstrated in high T_c superconductor $YBa_2Cu_3O_{7-\delta}$ thin film grown on miscut substrates, in which an unusually large transverse voltage was generated when laser illuminated on the surface of this film.[1] And then, it was proved that the unique TTE voltage effect was a special TE phenomenon which utilized the non-vanishing components in the off-diagonal term of the Seebeck tensor $\boldsymbol{S}$.[2-3] This effect had great potential versatile applications such as fast self-powered room temperature detectors,[4] waste heat recovery devices and laser power meters.[5-8] The pioneering researchers clarified that materials with TTE voltage effect must be have three essential factors: (i) specific crystallographic orientation (inclined crystal orientation), i.e. the orientation of the principal crystal axes are tilted from the surface normal [see Fig. 1(a) for details], (ii) anisotropy of the Seebeck coefficient $\Delta S = S_{ab} - S_c \neq 0$ (here treated as a scalar), and (iii) establishment of the temperature gradient $\nabla_z T$ along the out-of-plane (*z*-axis) direction. Based on the above description, Lengfellner *et al.* derived the TTE voltage U_y along transverse (*y*-direction) direction in *xy* plane of the film,[3] which is given by

$$U_y = \frac{l}{2}\left(S_{ab} - S_c\right)\sin\left(2\alpha\right)\nabla_z T = \frac{l}{2t}\Delta S \sin\left(2\alpha\right)\Delta T_z \qquad (1)$$

Here, *l* and *t* are the illuminated length and thickness of the film. According to this formula, the key factor is $\Delta S = S_{ab} - S_c$, that is, large transport anisotropy (in this case, ΔS) implies large TTE voltage effect. The natural layered materials usually exhibit large ΔS. Therefore, many of them such as $YBa_2Cu_3O_{7-\delta}$, $La_{2-x}Sr_xCuO_4$, $Bi_2Sr_2CaCu_2O_8$ and Ca_xCoO_2 have since been extensively studied to enhance their TTE voltage performance.[9-13] Most of them belong to high T_c superconductor and colossal magnetoresistance materials. However, traditional TE materials were rarely used to develop TTE voltage effect except recent researches about Ca_xCoO_2,[11, 13] which was a typical oxide TE materials presenting good TE and TTE performance due to their layered structure with large $\Delta S = 35\ \mu VK^{-1}$. In this case, excellent TTE voltage effect could be developed from traditional TE materials because they are both TE phenomenon. Heavy Nb-doped $SrTiO_3$ ($SrTi_{1-x}Nb_xO_3$, NSTO) epitaxial film is a promising candidate for developing TTE effect because it exhibits a rather large $\boldsymbol{S}$ due to the large density of states effective mass.[14] Nevertheless, with regard to TTE effect of NSTO epitaxial films, few works have been reported because they belong to 113 member of Ruddlesden-Popper family, which presents a relatively small anisotropy due to their cubic structure.[8] The only study was miscut NSTO single crystals, in which the voltage signals were observed only several millivolts.[15] More recently, Hiromichi Ohta *et al.* demonstrated that a high-density two-dimensional electron gas confined within a unit cell layer in $SrTiO_3/SrTi_{0.8}Nb_{0.2}O_3$

superlattices yielded an unusually large ***S***, approximately five times larger than that of the bulk $SrTiO_3$ (STO).[16]

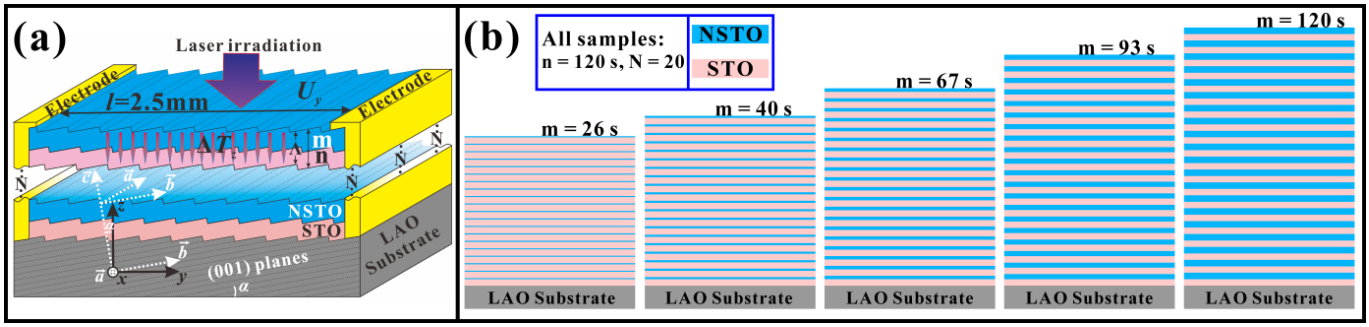

Fig. 1 Experimental configuration to develop the TTE effect: (a) The schematic cross-sectional view of the STO/NSTO multilayer films with inclined orientation is shown. *abc* and *xyz* are the crystal axes and the geometrical axes, respectively; (b) Sketch for the formula of STO/NSTO multilayer films.

To utilize the large ***S*** and further enhance the value of ΔS, here we focused on STO/NSTO artificial multilayer films which were alternately stacked by STO insulative sublayers and heavy doped NSTO conductive sublayers as shown in Fig. 1(b). In such sandwich structure, the electrons were confined between the two STO insulative layers. The electronic transport properties in *ab* plane were different from that in *c*-axis direction realizing anisotropy, namely, $\Delta S = S_{ab} - S_c$. What is more, the improved TTE effect has been observed in NSTO single layer epitaxial films with a tilted orientation in our previous report.[17] In this study, STO/NSTO artificial multilayer structure was fabricated to enhance the anisotropy for further improving the TTE effect. The epitaxial behavior and exact crystal orientation of the STO/NSTO multilayer films were confirmed. Based on that the TTE voltage effect of the samples were tested and investigated.

Experimental

Undoped STO and heavy doped NSTO (20% Nb doped, as the stoichiometric ratio) polycrystalline ceramics were prepared by solid-state sintering technique at 1250 °C, which were used as targets for STO/NSTO multilayer films deposition. The 10° off-cut (001)-oriented $LaAlO_3$ (LAO) single crystals with the size of 3 mm × 1.5 mm × 0.5 mm were used as the substrates. During the growth of multilayer films, the two home-made targets were alternately ablated by the pulsed laser deposition (PLD) system with a KrF excimer laser (wavelength is 248 nm, pulse width is 28 ns, energy density is ~1 $mJ \cdot mm^{-2} \cdot pulse^{-1}$, repetition rate is 5 Hz) at 820 °C in a flowing oxygen atmosphere. The flowing oxygen pressure was fixed at 1.0×10^{-2} Pa which not only made the NSTO sublayers keeping a high conductivity (n_e = ~10^{21} cm^{-3}), but also ensured the STO sublayers in a insulative state (n_e = ~10^{18} cm^{-3}) by preventing them from forming oxygen vacancies. Consequently, the multilayer structures of $[(STO)_n/(NSTO)_m]_N$ were constructed [Fig. 1(b)], where *n* and *m* represent the deposition time of the STO and NSTO sublayers and *N* is the total stacking periodic number. It should be noted that the deposition time were used as nominal thickness before the real thickness was confirmed. The designed thickness of NSTO sublayer ($t_{NSTO} = m \times v_{NSTO}$, *v* is deposition rate) was set at 26, 40, 67, 93, 120s, while the STO sublayer ($t_{STO} = n \times v_{STO}$) and *N* were set as the fixed value of 120s and 20, respectively. All films were *in situ* annealed for 0.5 h to decrease the amount of oxygen deficiency and improve the crystal quality. The periodic structure, crystal orientation and epitaxial relationship of the multilayer films were determined by special 2θ-θ scans of X-ray diffraction (XRD) and high-resolution transmission electron microscopy (HRTEM). Energy dispersive X-ray (EDX) testing was adopted to confirm the elements distributions and the Nb composition *x* in the films. After making the in-plane silver electrodes, the TTE voltage signals of STO/NSTO multilayer films were measured and recorded at room temperature using the home-built TTE voltage signal collection system.

Results and discussion

Fig. 2(a) shows the phase compositions of STO and NSTO targets verified by XRD, both of which present only one titanate phase with the typical perovskite structure. However, compared to STO (lattice parameter a_{STO} = 3.907 Å), the (110) peak of NSTO slightly shifted 0.07° to a lower angle [the inset of Fig. 2(a)]. The shifting suggests that the Nb atoms have been doped into the lattices of NSTO. Fig. 2(b) shows the XRD patterns of all STO/NSTO multilayer films deposited on 10° off-cut (001)-LAO substrates with different *m*. Since the (001) planes (namely, the *ab* planes of LAO shown in Fig. 1(a)) of LAO substrate was tilted by an angle of 10° with respect to the surface, the [001] axis of LAO must be aligned accurately and the offset point was set as $\omega = 10° = \alpha$ to satisfy the Bragg's diffraction geometry using the usual θ-2θ scan [see the inset of Fig. 2(b) for details]. Only intense Bragg XRD peaks of (00*l*) for both films and substrates were observed. The simultaneous presence of sharp (00*l*) peaks implies that the multilayer films had the same orientation as LAO substrates, that is, well-defined *c*-axis oriented films. For (002) peak of the films, there was only one peak when *m* was 26 s or 40 s, whereas it started to split into two peaks when *m* reached to 67s. The splitted peak located at the lower-angle is from NSTO and the other is from STO. This phenomenon is caused by the increasing content of the NSTO crystalline involved in the diffraction processing. On

the other hand, it is due to the crystal lattice expansion of partial substitution of Ti^{4+} by Nb^{5+} in the NSTO sublayers.

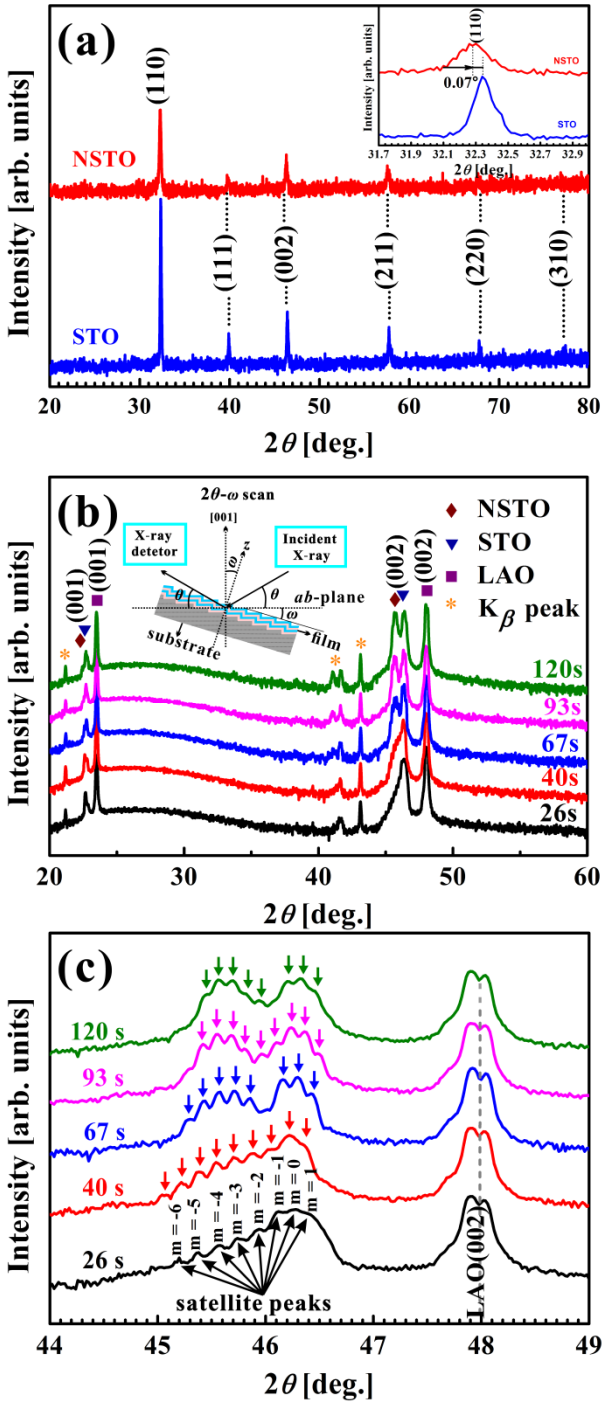

Fig. 2 (a) The XRD patterns of STO and NSTO polycrystalline ceramics targets. The inset shows the shifting around (110) peak of NSTO compared with that of STO; (b) The XRD patterns of all multilayer films revealing well-defined *c*-axis orientation. The inset displays the configuration of special XRD measurement; (c) The typical high angle satellite peaks appeared around (002) peaks marked with arrows.

At the same time, the pendellosung fringes can be clearly observed around the (002) peak in all samples, which are the satellite peaks from periodic modulation structure and the details are shown in Fig. 2(c). The presence of high-angle satellite peaks implies the multilayer films have atomically smooth interfaces and high-crystalline qualities. The satellite peak positions were marked by arrows, and the distance of the peaks became narrow gradually with increasing the value of *m*. The varied satellite peak positions suggest that the modulation length Λ is different from each other in these periodic structures. Using the angular positions of the satellite peaks, the theoretical modulation length ($\Lambda = t_{NSTO} + t_{STO} = m \times v_{NSTO} + n \times v_{STO}$) can be calculated by the formula,[18-19] $2\Lambda\sin\theta_i = i\lambda$, where λ is the wavelength of Cu (K_α) radiation and *i* is the order of the satellite peak. The value of Λ extracted from the slope of $\sin\theta_i$–*i* plot [see Fig. S1† for an example] are 50.3, 55.8, 66.4, 76.2, 85.6 nm for *m* = 26, 40, 67, 93, 120 s multilayer films, respectively. The obtained value of Λ are substituted into the equation of $\Lambda = t_{NSTO} + t_{STO} = m \times v_{NSTO} + n \times v_{STO}$, consequently, the calculated real thicknesses of NSTO sublayer are ~7 nm for *m* = 26 s, ~13 nm for *m* = 40 s, ~23 nm for *m* = 67 s, ~33 nm for *m* = 93 s, and ~43 nm for *m* = 120 s, respectively. And the thickness of STO sublayer keeps the value of 42.8 nm when *n* is fixed at 120 s. The deposition rate of NSTO is also determined as 0.348 $nm \cdot s^{-1}$ or 0.069 $nm \cdot pulse^{-1}$ from Fig. S2†. (Note that the real thicknesses will be used in the following text).

The composition was analysed by EDX along the growth direction (Fig. S3†). The contents of Nb and Ti atoms periodically alternated between ups and downs along the growth direction, whereas the profiles of Sr and O always showed a straight line without any fluctuation in the whole testing region. It is concluded that the multilayer films are periodic modulated structure and the site of Ti^{4+} (0.605 Å) has been successfully substituted by Nb^{5+} (0.64 Å). The EDX testing also verifies that the Nb composition *x* of NSTO sublayer is nearly ~0.15.

To further confirm the above results of XRD and better understand the crystal orientation as well as epitaxial relationship, the cross-sectional TEM analysis was conducted in the order from low to high magnification in *zy* plane of the specimens. The low magnification bright-field (BF) TEM images for the sample of *m* = 67 s is shown in Fig. 3(a). In the view area, it shows bright/dark alternating layered structure feature and clean interfaces without intermixing and grain boundaries, confirming the 2D growth model of the film along *z* direction. The NSTO and STO sublayer thicknesses are exactly determined to be ~23 nm and ~43 nm, respectively. It is well agreement with the XRD calculation values. The corresponding selected area electron diffraction (SAED) pattern obtained from the film region is shown in the inset of Fig. 3(a). The distinguished sharp diffraction spots indicate the multilayer films are consisted of high quality STO and NSTO single-crystal epitaxial layers. It can be seen that the diffraction spots are sharp for those with lower indices. However, they start to split to two dots from those with higher indices. The magnified image of (002) spot, for instance, is displayed in the inset of SAED pattern. The pattern near the (000) point belongs to the

NSTO layers and the other one belongs to the STO layers since the lattice parameters of NSTO are larger than that of STO. Moreover, the splitted two spots and (000) point are almost in the same straight line in the reciprocal space. The phenomenon illustrates that the spots splitting is resulted from lattice expansion in *c*-axis direction in some local areas close to the STO/NSTO interfaces, rather than crystal orientation difference existing between the STO and NSTO sublayers. As a result, it can be concluded that the STO and NSTO layers are epitaxially grown alternatively without orientation variation between each other.

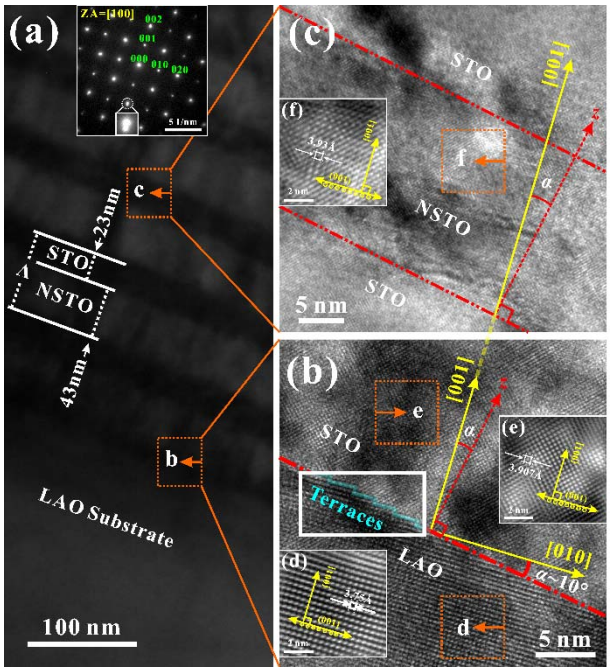

Fig. 3 Cross-sectional TEM studies in *zy*-plane showing the orientation relationship and epitaxial behavior of STO/NSTO multilayer films on 10° off-cut (001) LAO substrate: (a) a low magnification BF image near the film/substrate interface, the inset of (a) showing SAED pattern from the film area; (b), (c) the magnified views of LAO/STO and STO/NSTO/STO interfaces from the regions b and c; The HRTEM images of (d) LAO, (e) STO and (f) NSTO indicating the uniform crystal orientation.

Fig. 3(b) and (c) show the representative TEM images of the LAO/STO interface and STO/NSTO/STO interface, respectively, which are magnified from the regions b and c of Fig. 3(a). In the LAO/STO interface area, it can be clearly observed that alternating terraces with several atoms wide are separated by a train of atomic-height steps. The terraces and (001) planes are coplanar, which have an inclined orientation with an angle of α = 10° against the LAO/STO interface (red dash dot line). In the meantime, the atoms on (001) planes along [010] axis of the STO layer are aligned and also form a tilted angle of α = 10° with the LAO/STO interface. It is suggest that the *c*-axis ([001] direction) of the STO layer is rotated 10° with respect to the normal direction of the LAO/STO interface (*z*-direction). Therefore, the STO layer is epitaxially grown in off-step-terrace flow mode on LAO substrate with inclined (001) planes exactly tilted away from the interface by 10°, following the 10° off-cut angle of LAO substrate. For STO/NSTO/STO interface area, both the [001] axes of STO and NSTO layers place in line with the extended line of [001] axis of the first STO layer, also forming 10° angle with respect to the normal direction of STO/NSTO and NSTO/STO interfaces (red double dot dash line). It means that the NSTO layer is epitaxially grown on the STO layer with the same crystal orientation. Parts (d)-(f) of Fig. 3 show the high resolution HRTEM images of the selected small area in LAO substrate, STO layer and NSTO layer, respectively. In the three single-crystal layers, not only the atoms on (001) planes (yellow circles) are parallel to each other but also the three [001] axes are in one straight line, again confirming that each layer has the same inclined orientation. Based on the above TEM results, the out-of plane and in-plane orientation relationship of the STO/NSTO multilayer films are determined to be 10°-off-$(001)_{NSTO}$‖10°-off-$(001)_{STO}$‖10°-off-$(001)_{LAO}$ and 10°-off-$[110]_{NSTO}$‖10°-off-$[110]_{STO}$‖10°-off-$[110]_{LAO}$. In addition, the lattice constants of LAO, STO and NSTO along [001] and [010] direction were measured by the HRTEM images. These layers are still cubic structure with the lattice constants of ~3.75 Å, ~3.905 Å and ~3.93 Å, respectively.

In order to obtain the unusual TTE voltage signals and elucidate the TTE voltage properties of the STO/NSTO multilayer films, we have measured and collected the corresponding voltage signals along *x* and *y* directions named as U_x and U_y, respectively, using the home-built equipment as shown in Fig. 4(a). It is worth noting that the ultraviolet laser with wavelength of 248 nm and pulse width of 28 ns was used as the heat source to generate the temperature gradient $\nabla_z T$ along the out-of-plane direction of the film. The laser beam shape was adjusted to a rectangle with the size of 30 mm × 10 mm to ensure the whole film was illuminated in the laser spot. The maximum illumination size of the film was 2.5 mm × 1.5 mm after deducting the area occupied by the silver electrodes. And thus the on-film energy E_a (the energy absorbed by the film) was only a few tenths of a millijoule to a few millijoules.

It has well achieved our expectation that the TTE voltages exceeding several hundreds of millivolts have been observed in such artificial STO/NSTO multilayer films with inclined crystal orientation. The unusual TTE voltage in these films are hundreds times larger than the miscut Nb-doped $SrTiO_3$ (~ 3 mV) single crystals previously reported.[15] Fig. 4(b) shows the typical time dependence of TTE voltage signals waveform of a STO/NSTO multilayer film with $t_{NSTO} \approx 23$ nm at $E_a = 3.94$ mJ. The peak value of transverse voltage U_y (line with wine solid ball) approaching nearly 0.744 volts (U_p = 0.744 V) was measured along the *y* direction while in complete contrast to the *x* direction, a quite small voltage U_x close to zero (line orange open circles) was observed. This phenomenon can be explained that the component of the tilted *c*-axis is totally projected along the *y* direction, where the crystal orientation is tiled (α = 10°) but the *x* direction is not (α = 0°). This is why we call this phenomenon as transverse TE voltage effect. The observed large TTE voltage proves that the artificial multilayer films

structure with special inclined crystal orientation is effective to develop the TTE voltage effect, despite the multilayers consisted of cubic structure materials with a relatively small ΔS.

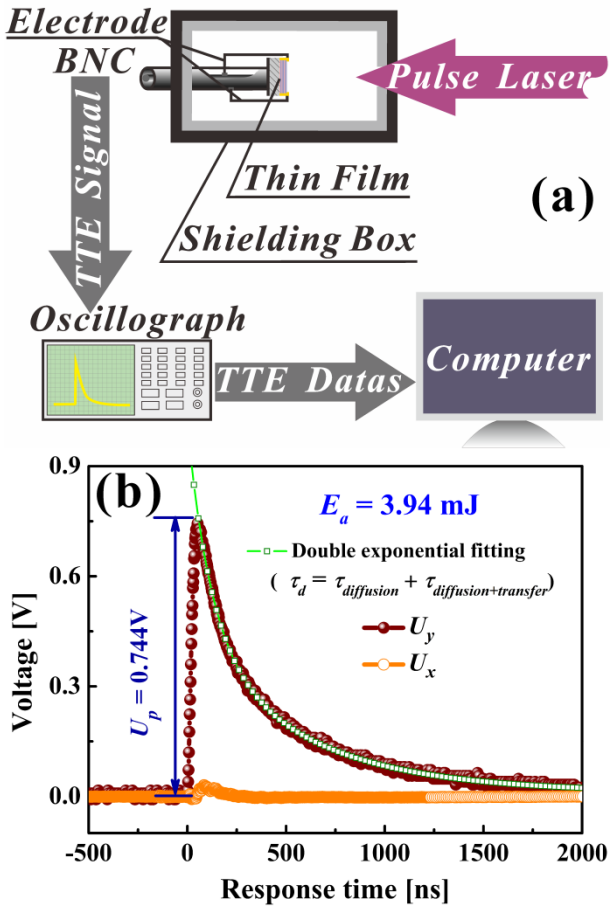

Fig. 4 (a) The TTE voltage signal collection system; (b) Typical time dependence of TTE voltage signals of a STO/NSTO multilayer film with t_{NSTO} ≈ 23 nm at E_a = 3.94 mJ along *x* direction and *y* direction.

On the other hand, a $\Delta S \cdot \nabla_z T$ of 1740 mV·mm^{-1} is exhibited in this sample, which is far greater than that in the bulk single-crystal NSTO (17.5 mV·mm^{-1}) with the same inclined crystal orientation (10°). However, the estimated $\nabla_z T$ in the two systems have the same order of magnitude because both the illuminated lasers are UV-laser with almost equivalent energy density and laser penetration depth.[12, 20] Thus, the estimated value of $\nabla_z T$ is ~10^2 K·m^{-1} according to the equation of $\nabla_z T \simeq E_a/(K_z \cdot \tau_{dif})$,[21] where τ_{dif} is the thermal diffusion time, K_z is the thermal conductivity perpendicular to the film surface. The associated parameters are shown in Table 1. This suggests that the enhanced ΔS of ~11.8 μV/K has been achieved in these STO/NSTO multilayer films. It can be concluded that the layered confined structure with inclined crystal orientation play an important role to induce the anisotropy of transport properties between in-plane and out-of-plane. It enhances the value of ΔS, and then further improves the TTE effect in such artificial multilayer films.

Table 1 Comparison of relative parameters of bulk NSTO and STO/NSTO multilayer film.

Materials	U_y (mV)	E_a (mJ)	l (mm)	α (°)	K_z (W·m^{-1}·K^{-1})	$\Delta S \cdot \nabla_z T$ (mV·mm^{-1})
NSTO[a]	3	5.35	1	10	8.8[b]	17.5
STO/NSTO[c]	744	3.94	2.5	10	10.2	1740

[a] Reference 15, [b] Reference 14, [c] Presented in this work.

At same time, the TTE voltage signal also displays a fast response time with the magnitude of several hundred nanoseconds. It can be clearly seen that the response time of the voltage signal consists of one sharp rising edge and another gradual decay edge from the asymmetric voltage waveform shown in Fig. 4(b). For rising edge time (τ_s), all films exhibit a short τ_s ranging from ~20 ns to ~30 ns, which is almost constant and approximately equal to the laser pulse width (= 28 ns). Whereas, for decay edge time (τ_d), a variable depending on how fast the thermal equilibrium established, is related to the time spent on thermal relaxation. Therefore, the response time is mainly affected by τ_d. In this case, the signal decay behavior can be described by the time dependence of thermal model.[12, 20] Fig. 4(b) shows the simulated decay edge waveform (line with green squares), exhibiting a good double-exponential decay. The simulated decay curve is then expressed by the double-exponential function, $A_{fast}\exp(-t/\tau_{fast}) + A_{slow}\exp(-t/\tau_{slow})$. Here, A_{fast} and A_{slow} are constants; τ_{fast} and τ_{slow} are the decay time components. The double exponential decay behavior implies that the thermal relaxation mechanism includes two stage processes in these multilayer films.

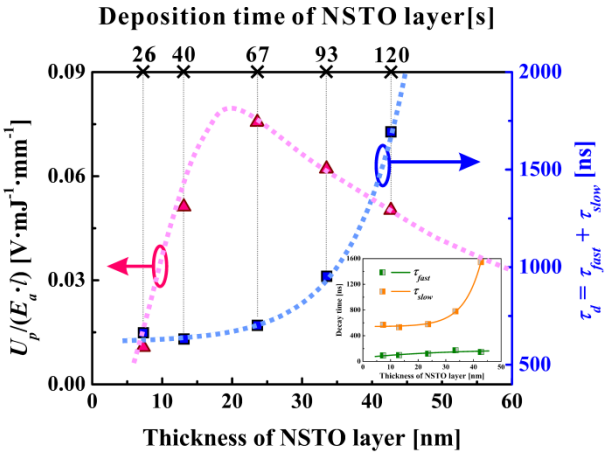

Fig. 5 Thickness of NSTO layer t_{NSTO} dependence of the magnitude of $U_p/(E_a \cdot l)$ and τ_d, respectively. The dashed lines are used for guiding the trend. The inset shows the relation between two decay time components and t_{NSTO}.

It is necessary to further investigate the unique TTE voltage effect in STO/NSTO multilayer films in consideration of the potential applications due to their large voltage signals and adjustable response time. Fig. 5 shows the U_p normalized by E_a and l as a function of t_{NSTO}. It is found that the $U_p/(E_a \cdot l)$ showed a monotone increase firstly, and then dropped gradually with further increasing the value of t_{NSTO}. The value of $U_p/(E_a \cdot l)$ reaches to 0.076 V·mJ^{-1}·mm^{-1} when t_{NSTO} is about 20 nm. It is

more than three times larger than our previous research in the NSTO single layer film which is only ~0.02 $V \cdot mJ^{-1} \cdot mm^{-1}$ when the thickness of film decreased to ~20 nm.[17] The comparison result demonstrates that photo-thermal conversion efficiency can be further improved by the multilayer structure with the same NSTO layer. The emerged peak around t_{NSTO} = 20 nm in the $U_p/(E_a \cdot l)$-t_{NSTO} curve indicates that an optimum film thickness is corresponding to a maximum TTE voltage, that is the maximum conversion efficiency, does exist. However, the maximum U_p would not appear around t_{NSTO} = 20 nm because U_y is in direct proportion to $1/t$ according to equation (1), in other word, the maximum U_p will be obtained when the sample is a very thinner film ($t \rightarrow 0$). For this contradiction, a reasonable explanation is presented using the formula of time dependence of TTE voltage which can be written as[22]

$$U_y(\tau) = \frac{\alpha_0 E_a l \Delta S \sin 2\alpha}{4t\rho c\sqrt{\pi D\tau}}\left(e^{\delta^2/4D\tau} - e^{t^2/4D\tau}\right) \quad (3)$$

where, α_0, ρ, δ, c, τ, and D are absorption coefficient, density, laser penetration depth, specific heat, response time, and thermal diffusivity of the film, respectively. All other parameters share the same definition with equation (1). Equation (3) can be viewed as a function of t rather than the simple relation of $1/t$ mentioned in equation (1). To certify the existence of the maximum U_y, one partial differential equation regarding to t is obtained from equation (3)

$$\frac{\partial^2 U_y}{\partial t^2} = \frac{2A}{t^3}[e^{-\delta^2 B} - e^{-t^2 B}] - \frac{2AB}{t}e^{-t^2 B} - 4AB^2 t e^{-t^2 B} \quad (4)$$

In the above expression,

$$A = \frac{\alpha_0 E_i l \sin(2\alpha)}{4\rho c_0\sqrt{4\pi D\tau}}\Delta S > 0; B = \frac{1}{4D\tau} > 0 \quad (5)$$

Obviously, $\partial^2 U_y/\partial t^2 < 0$ illustrates that there is a maximum of U_p when t takes a certain value (here is t_{NSTO}). And this proves the presence of optimum thickness, which is consistent with the measured results as shown in Fig. 5.

The profile of τ_d composed from the decay time components τ_{fast} and τ_{slow} versus t_{NSTO} also is presented in Fig. 5, which shows a relationship of exponential increase. The τ_d transition occurs when t_{NSTO} is larger than ~20 nm. The inset of Fig. 5 shows the variation trends of τ_{fast} and τ_{slow} with the change of t_{NSTO}, from which we see that τ_{fast} was slightly affected by t_{NSTO} and increased only from ~94 to ~150 ns. On the other hand, τ_{slow} was greatly affected by t_{NSTO} and it increased exponentially from ~530 to ~1550 ns. The results indicate that the stage reflected by τ_{fast} is a fast heat propagation process governed by only heat diffusion, where the thermal energy is delivered by the laser because heat diffusion length is as short as the laser penetration depth (~ 100 nm). In this stage, due to the short heat diffusion length, the thermal energy is scattered by only two to three interfaces so as to present a small value of τ_{fast} and a slight variation in this t_{NSTO} range. However, when the thermal energy is delivered to the deeper area within the film by the fast stage, the other lagged and relative slow stage reflected by τ_{slow} will happen. This stage is governed by concurrent free heat diffusion and transfer, where the heat flux diffuses and transfers for a long distance to the bottom of the film (film/substrate interface) until the system reaches to thermal equilibrium (ΔT_z dropped to zero). It means that the thermal energy is multiply scattered by the interfaces, and the thermal equilibrium is slowly established so as to present a large value of τ_{slow} and a great variation in this t_{NSTO} range. The results suggest that τ_d can be regulated by controlling the thickness of NSTO layer and number of heat scattering interfaces, thereby adjusting the response time. In addition, it should be noted that the optimum match of the largest U_p with faster response time appeared around $t_{NSTO} \approx$ 20 nm in our material system according to Fig. 5.

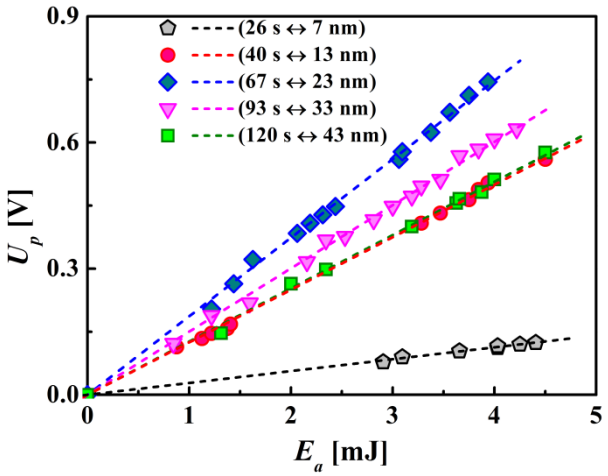

Fig. 6 E_a dependence of U_p for each film. Dashed lines represent linear fits to the data in the E_a range.

Fig. 6 shows the varied magnitude of U_p and on-film absorbed laser energy E_a for different t_{NSTO}. The measured values of U_p have a good linear relation with E_a for each film, which suggests that U_p is proportional to E_a as shown by the dash line. However, E_a is not involved in equation (1). That is because the dependence of E_a on ΔT_z ($\Delta T_z \propto E_a$) can be deduced by the one-dimensional heat diffusion model.[20] As a result, Fig. 6 expresses an interrelation of $U_p \propto \Delta T_z \propto E_a$, which is in excellent agreement with equation (1).

All these aforementioned results suggest that high sensitivity, fast response light/heat detector and laser power elements can be designed by utilizing the properties of the large voltage signal, adjustable response time and well linear relationship between them.

Conclusions

Artificial STO/NSTO multilayer films were epitaxially grown on 10° off-cut (001) LAO substrates by PLD. The microstructure investigation from XRD and HRTEM indicated that each sublayer had an inclined (001) plane in strict

accordance with 10° against the interfaces. The orientation relationships between out-of-plane and in-plane are 10°-off-$(001)_{NSTO}$‖10°-off-$(001)_{STO}$‖10°-off-$(001)_{LAO}$ and 10°-off-$[110]_{NSTO}$‖10°-off-$[110]_{STO}$‖10°-off-$[110]_{LAO}$, respectively. Comparing with the bulk single-crystal NSTO with the same inclined orientation, a larger TTE voltage obtained indicate that constructing the artificial STO/NSTO multilayer structure is an effective method to improve the TTE voltage effect due to the enhanced ΔS. In addition, the response time can be adjusted by controlling the thickness of NSTO sublayer, and the value of U_p also presented a significant linear relation with E_a. All the results demonstrate that based on the artificial multilayer structure, more material designs for potential versatile applications shall be provided.

Acknowledgements

This work was supported by the National Natural Science Foundation of China (Grant No. 51272205, 51072157, 51302208), by Doctoral Fund of Ministry of Education of China (Grant No. 20130201120003), by China Postdoctoral Science Foundation (Grant No. 2012M521763), and by the Fundamental Research Funds for the Central Universities (Grant No. xjj2013110).

Notes and references

[a] State Key Laboratory for Mechanical Behavior of Materials, Xi'an Jiaotong University, Xi'an, 710049, China.
E-mail: qinyi.andy@gmail.com;
Fax: +86 029 8266 7942-804; Tel: +86 029 8266 7942-803;
[b] Institute of Advance Materials for Photoelectronics, Kunming University of Science and Technology, Kunming, 650051, China.
E-mail: pxzhang@fkf.mpg.de
[c] Max Planck Institute for Solid State Research, Heisenbergstrasse 1, Stuttgart, D-70569, Germany.

† Electronic Supplementary Information (ESI) available: Graphical determination of the modulation length Λ and the deposition rate of NSTO; The distribution of Sr, Ti, Nb and O along the epitaxial direction. See DOI: 10.1039/b000000x/

1 C. L. Chang, A. Kleinhammes, W. G. Moulton, L. R. Testardi, *Phys. Rev. B*, 1990, **41**, 11564.
2 H. Lengfellner, G. Kremb, A. Schnellbogl, J. Betz, K. F. Renk, W. Prettl, *Appl. Phys. Lett.*, 1992, **60**, 501.
3 H. Lengfellner, S. Zeuner, W. Prettl, K. F. Renk, *Europhys. Lett.*, 1994, **27**, 491.
4 K. Fischer, C. Stoiber, A. Kyarad, H. Lengfellner, *Appl. Phys. A: Mater. Sci. Process.*, 2004, **78**, 323.
5 T. Kanno, A. Sakai, K. Takahashi, A. Omote, H. Adachi, Y. Yamada, *Appl. Phys. Lett.*, 2012, **101**, 011906.
6 T. Kanno, S. Yotsuhashi, A. Sakai, K. Takahashi, H. Adachi, *Appl. Phys. Lett.*, 2009, **94**, 061917.
7 S. Wang, S. Chen, F. Liu, G. Yan, J. Chen, H. Li, J. Wang, W. Yu, G. Fu, *Appl. Surf. Sci.*, 2012, **258**, 7330.
8 P. X. Zhang, H.-U. Habermeier, *J. Nanomater.*, 2008, **2008**, 329601.
9 F. Xiong, H. Zhang, Z. M. Jiang, P. X. Zhang, *J. Appl. Phys.*, 2008, **104**, 053118.
10 T. Zahner, R. Stierstorfer, R. Rössler, J. D. Pedarnig, D. Bäuerle, H. Lengfellner, *Physica C: Superconductivity*, 1998, **298**, 91.
11 K. Takahashi, A. Sakai, T. Kanno, H. Adachi, *Appl. Phys. Lett.*, 2009, **95**, 051913.
12 K. Takahashi, T. Kanno, A. Sakai, H. Adachi, Y. Yamada, *Phys. Rev. B*, 2011, **83**, 115107.
13 K. Takahashi, T. Kanno, A. Sakai, H. Adachi, Y. Yamada, *Appl. Phys. Lett.*, 2010, **97**, 021906.
14 H. Ohta, K. Sugiura, K. Koumoto, *Inorg. Chem.*, 2008, **47**, 8429.
15 N. Zhou, K. Zhao, H. Liu, Z. Lu, H. Zhao, L. Tian, W. Liu, S. Zhao, *J. Appl. Phys.*, 2009, **105**, 083110.
16 H. Ohta, S. Kim, Y. Mune, T. Mizoguchi, K. Nomura, S. Ohta, T. Nomura, Y. Nakanishi, Y. Ikuhara, M. Hirano, H. Hosono, K. Koumoto, *Nat Mater*, 2007, **6**, 129.
17 Y. Qin, T. Zhao, H.-H. Zhang, B. Wang, P.-X. Zhang, J.-F. Yang, *Appl. Phys. Lett.*, 2013, **102**, 253901.
18 L. Qiao, X. Bi, *CrystEngComm*, 2011, **13**, 1693.
19 J. C. Rojas Sánchez, M. Granada, L. B. Steren, I. Mazzaro, D. H. Mosca, *Appl. Surf. Sci.*, 2007, **254**, 219.
20 S. Zeuner, H. Lengfellner, W. Prettl, *Phys. Rev. B*, 1995, **51**, 11903.
21 T. Zahner, R. Forg, H. Lengfellner, *Appl. Phys. Lett.*, 1998, **73**, 1364.
22 P. X. Zhang, W. K. Lee, G. Y. Zhang, *Appl. Phys. Lett.*, 2002, **81**, 4026.